

## A Preprint

ORIGINAL VERSION SUBMITTED ON NOVEMBER 30, 2025

## A Neuromodulable Current-Mode Silicon Neuron for Robust and Adaptive Neuromorphic Systems

Loris Mendolia<sup>1,\*</sup>, Chenxi Wen<sup>2</sup>, Elisabetta Chicca<sup>3</sup>, Giacomo Indiveri<sup>2</sup>, Rodolphe Sepulchre<sup>4</sup>, Jean-Michel Redouté<sup>1</sup> and Alessio Franci<sup>1,5,\*</sup><sup>1</sup>Department of Electrical Engineering and Computer Science, University of Liège, Liège, Belgium<sup>2</sup>Institute of Neuroinformatics, University of Zurich & ETH Zurich, Zurich, Switzerland<sup>3</sup>Bio-Inspired Circuits and Systems Lab, Zernike Institute for Advanced Materials & Groningen Cognitive Systems and Materials Center, University of Groningen, Groningen, The Netherlands<sup>4</sup>Department of Engineering, University of Cambridge, Cambridge, U.K. & Department of Electrical Engineering, KU Leuven, Leuven, Belgium<sup>5</sup>WEL Research Institute, Wavre, Belgium

\*Authors to whom any correspondence should be addressed.

**E-mail:** [lmendolia@uliege.be](mailto:lmendolia@uliege.be), [afranci@uliege.be](mailto:afranci@uliege.be)**Keywords:** Neuromorphic engineering, Silicon neurons, Neuromodulation, CMOS analog circuits, Current-mode design**Abstract**

Neuromorphic engineering makes use of mixed-signal analog and digital circuits to directly emulate the computational principles of biological brains. Such electronic systems offer a high degree of adaptability, robustness, and energy efficiency across a wide range of tasks, from edge computing to robotics. Within this context, we investigate a key feature of biological neurons: their ability to carry out robust and reliable computation by adapting their input response and spiking pattern to context through neuromodulation. Achieving analogous levels of robustness and adaptation in neuromorphic circuits through modulatory mechanisms is a largely unexplored path. We present a novel current-mode neuron design that supports robust neuromodulation with minimal model complexity, compatible with standard CMOS technologies. We first introduce a mathematical model of the circuit and provide tools to analyze and tune the neuron behavior; we then demonstrate both theoretically and experimentally the biologically plausible neuromodulation adaptation capabilities of the circuit over a wide range of parameters. All the theoretical predictions were verified in experiments on a low-power 180 nm CMOS implementation of the proposed neuron circuit. Due to the analog underlying feedback structure, the proposed adaptive neuromodulable neuron exhibits a high degree of robustness, flexibility, and scalability across operating ranges of currents and temperatures, making it a perfect candidate for real-world neuromorphic applications.

**1 Introduction**

The remarkable efficiency and adaptability of the human brain emerge not only from the dynamics of spiking neurons and plastic synapses, but also from a cellular regulation mechanism known as neuromodulation [1–4]. Neuromodulators, such as dopamine and serotonin, shape neuronal behavior over timescales ranging from seconds to minutes by adjusting excitability, firing thresholds and spiking patterns, and by regulating rhythmic activity [5]. The study of the role of neuromodulation for shaping rhythmic circuits, and in particular central pattern generators (CPGs), has provided fundamental insights into how neural systems achieve quick and robust adaptability to changing environment. This ability to flexibly switch between behaviors without structural rewiring of neuronal circuits can be a powerful, yet largely unexplored source of inspiration for neuromorphic hardware design [6].

The opportunities provided by neuromodulation are illustrated in Figure 1. The top traces are physiological recordings of a neuron undergoing neuromodulation, switching between slow tonic spiking and a transient bursting. The first mode supports linear rate-based encoding of the input strength, while the second allows a nonlinear detection of input changes, or a "wake-up call"

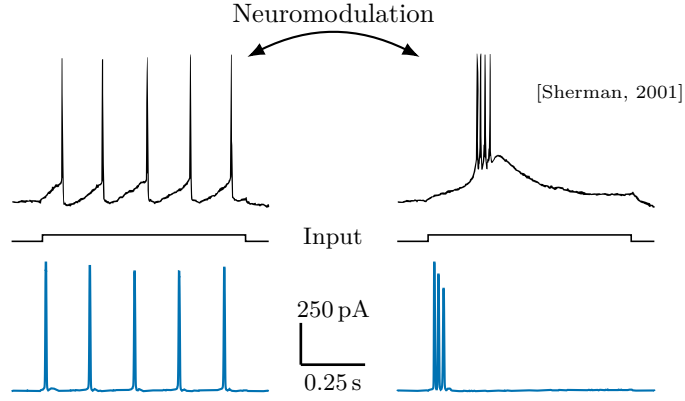


**Figure 1.** Neuromodulation in thalamocortical relay neurons (top, adapted from [7]) vs. neuromodulation recorded in our silicon neuron (bottom). For the same input current step (middle trace), neuromodulation enables a switch between tonic spiking (left) and a single transient burst (right), corresponding respectively to a linear rate-based encoding or a nonlinear "wake-up call" response to changes. Subthreshold integration dynamics are also reproduced in our neuron, but are much faster than biological neurons due to the limited capacitor sizes.

response. The bottom traces show the same modulation recorded experimentally on our neuromorphic chip presented in this work, where varying a single bias voltage enables reliable behavioral switches across all neurons present on chip. Capturing such transitions in silicon not only brings us closer to the richness of biological computation, but also enables a new range of possibilities for flexible and adaptive behaviors in neuromorphic systems. This example is one of many possibilities for functional switches in behaviors achievable using neuromodulation.

Neuromorphic engineering aims to replicate neural computation using analog, digital, or mixed-signal circuits that mimic the asynchronous, event-driven, and massively parallel architecture of the brain [8–13]. In the analog and mixed-signal domains, subthreshold transistor operation and current-mode designs have naturally emerged as powerful techniques for implementing power-efficient circuits emulating neuronal dynamics [10, 14]. Subthreshold circuits exploit the exponential current-voltage relationship of field-effect transistors (FETs) near the threshold voltage to generate nonlinearities at ultra-low currents, while current-mode design allows direct addition and subtraction of signal, several orders of magnitude of current ranges despite limited voltage headrooms [8]. Most modern silicon neuron designs for large-scale analog and mixed-signal implementations are based on variations of compact integrate-and-fire (I&F) models [15, 16]. Their efficiency, robustness, and compactness make them highly scalable, but come at the cost of missing most of the key dynamical features needed to emulate biological neuromodulation in silicon, and reproduce richer behaviors such as robust bursting, rest-spike bistability, or rebound spiking and bursting. More than biological curiosities, these features play a central role in creating diverse temporal patterns, enabling context-dependent information processing, and supporting the emergence of different behavioral states. These rich behaviors, and the ability to flexibly switch between them, are crucial for tasks like robust locomotion, rhythmic pattern generation, sensory filtering, or behavioral switching [3, 5]. Reproducing this range of dynamical behaviors in compact and low-power neuromorphic hardware remains a challenge to date, as it involves using larger neuron models containing various nonlinear interactions between a larger number of state variables across multiple timescales. Some works have started addressing this issue [17–19], but do not achieve the level of integration and power efficiency that large scale integration requires.

Nevertheless, both neuroscience and neuromorphic computing communities increasingly recognize the computational and functional benefits of bursting dynamics and neuromodulation in neural systems. Bursting capabilities have been shown to be useful to enhance the performance of artificial spiking neural networks and learning tasks [20–23], and translating the robust and tunable rhythmic properties of CPGs into hardware has been the focus of several recent works [19, 24–27]. However, current analog and mixed-signal neuromorphic platforms (such as [28–30]) lack native and robust support for intrinsic bursting and neuromodulation, and the cited hardware examples rely instead on generating population-level emergent rhythms from large groups of spiking neurons, or exploiting biologically implausible dynamical features. Such strategies are typically non-robust or resource-intensive, limiting their practicality in real-world applications. The only exception to date is the neuron implementation in [19], though it operates in voltage mode and lacks the dynamic range and efficiency of current-mode subthreshold design.

Recently, "mixed-feedback" models have emerged as a promising tool to address the trade-off

between biological plausibility, model richness, and hardware viability by summarizing the complex ion channel kinetics of a neuron into a superposition of positive and negative feedback loops on a well-defined hierarchy of timescales [19, 31–35]. These models produce rich and controllable neuronal behaviors while remaining low-dimensional and tractable. Their reduced structure not only opens the door for plausible large-scale implementation of neuromodulable neurons, but also makes them more tractable for systematic analysis and tuning, as highlighted in [34].

In this work, we bridge the gap between the theoretical richness of mixed-feedback models and state-of-the-art analog neuromorphic circuit design. We present an implementation of a fully analog mixed-feedback neuromodulable neuron using current-mode subthreshold circuits [10, 36, 37]. Our design preserves the core dynamical structure of mixed-feedback models while introducing a series of practical improvements for hardware implementation, such as a positive feedback inactivation mechanism for reduced power consumption. The resulting circuit exhibits the ability to finely control the neuron’s firing regime while remaining compact and low-power. This approach lays the foundation for scalable neuromorphic systems that can exploit circuit-level neuromodulation for adaptive behavior tuning and context-aware computation in real-world tasks.

In Section 2, we introduce the proposed mixed-feedback neuron model and its current-mode implementation using subthreshold Complementary Metal-Oxide-Semiconductor (CMOS) circuits for a compact, modular and ultra-low-power hardware realization of a neuromodulable neuron. In this model, the different timescales are continuously coupled, as opposed to only being linked by events. This subtle difference drastically enhances the expressivity of our model. We detail the use of differential-pair integrator (DPI) [38] and current-mode sigmoid blocks, including a biologically inspired positive feedback inactivation mechanism. We also present a theoretical analysis framework connecting circuit-level tuning and model equations, adapted from previous works, to predict and control the spiking, bursting and other types of excitability that the neuron can display. In Section 3, we present experimental results obtained from a 180 nm CMOS prototype and our measurement setup, demonstrating robust spiking, bursting, and neuromodulation. We further validate the circuit’s resilience to temperature changes (5 to 45 °C) and report an energy efficiency of 40 to 200 pJ/spike at a 1.8 V supply. In Section 4, we discuss the role of slow positive feedback for robust bursting, further motivating our mixed-feedback approach, and compare our design with state-of-the-art bursting neuron implementations. Finally, Section 5 concludes the paper and outlines future research directions.

## 2 The mixed-feedback neuron circuit

To capture the essential dynamics of neuronal excitability and neuromodulation and implement them efficiently in hardware, we adopt a mixed-feedback approach [19, 31, 32, 34, 35], that uses a superposition of positive and negative feedbacks across distinct timescales. In contrast to the few existing mixed-feedback neuron implementations [19, 34], we propose a mixed-feedback architecture using current-mode circuits, ensuring more compact, robust, and energy efficient designs [10]. All state variables, such as the membrane potential and the various positive and negative feedback terms, are therefore represented as physical currents. This choice naturally supports the modularity of the feedback design, since the current-mode approach enables straightforward implementation of sum and difference operations through Kirchhoff’s current law. It is also particularly well suited to ultra-low power subthreshold CMOS circuits, even in technology nodes with limited voltage headroom [36, 37].

This section introduces the structure of our mixed-feedback neuron model and its specificities, details its implementation using subthreshold current-mode CMOS circuits, and presents a mathematical formulation for the analysis and tuning of the circuit.

### 2.1 A current-mode mixed-feedback neuron model

The design of a mixed-feedback architecture requires two distinct types of elements: first-order low-pass filters, and static sigmoidal functions.

A first order current-mode low-pass filter, with input  $I_{\text{in}}$  and output  $I_{\text{out}}$ , is described in state-space representation as

$$\tau \dot{I}_{\text{out}} = -I_{\text{out}} + G I_{\text{in}}, \quad (1)$$

where  $\tau$  is the time constant of the filter and  $G$  its gain. In the Laplace domain, (1) is represented by the transfer function

$$\frac{I_{\text{out}}}{I_{\text{in}}} = H(s) = \frac{G}{\tau s + 1},$$

with  $s$  the complex variable of the Laplace domain.

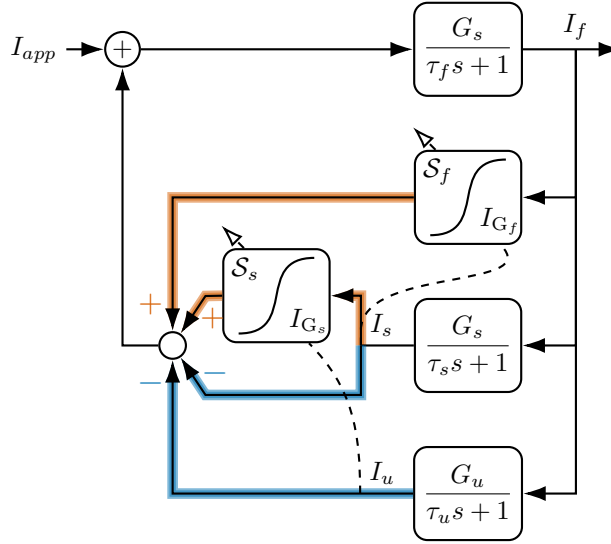


**Figure 2.** Mixed-feedback neuromodulable neuron structure. Red (*resp.* blue) highlighted arrows indicate positive (*resp.* negative) feedback paths. The symbols and circuit implementations of the two types of blocks are detailed in Figs. 4 and 5. The low-pass filter blocks are denoted using their transfer function, and the sigmoid blocks using the shape of their steady-state response. The dashed arrows represent the positive feedback inactivation illustrated in Fig. 3.  $I_f$  is the current-mode analog of the membrane potential.  $I_s$  and  $I_u$  respectively provide slow repolarization and ultraslow spike-frequency adaptation currents. The nonlinear sigmoid blocks provide positive feedback to create the fast spike upstroke and slow regenerative dynamics.

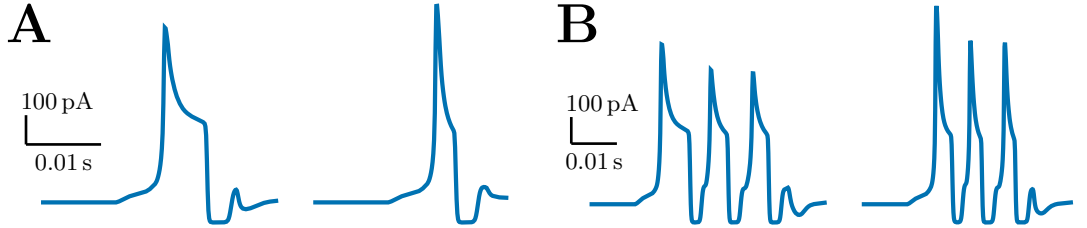


**Figure 3.** Spike (A) and burst (B) with (right) and without (left) positive feedback inactivation. The temporal extent of spikes and bursts is reduced thanks to the inactivation, but they remain long enough in time to directly signal to physical systems (in the spirit of [41]).

Examples of static sigmoidal current-mode input-output characteristics  $I_{\text{out}} = \mathcal{S}(I_{\text{in}}; I_G)$ , where  $I_G$  is the sigmoid gain, are shown in Fig. 6. The circuit implementations of both types of blocks are discussed in Section 2.2.

Given these two building blocks, the structure of our mixed-feedback neuron is represented in Fig. 2 using the block diagram representations introduced in Figs. 4 and 5. The internal dynamics of the model are organized around three low-pass filters defining three distinct timescales (fast, slow and ultraslow), two linear negative feedback loops (highlighted in blue) and two nonlinear positive feedback loops (highlighted in orange).

The fast low-pass filter takes the role of a leaky integrator and models the passive membrane dynamics of the neuron. Its output, the current  $I_f$ , serves as the current-mode analog of the neuron’s membrane potential. It receives the external inputs  $I_{\text{app}}$  to the neuron and integrates the effects of all the feedback loops, including the self-positive feedback loop through  $\mathcal{S}_f$ . The two other low-pass filters define the slow and ultraslow current-mode state variables  $I_s$  and  $I_u$ .  $I_s$  provides both linear slow negative feedback and nonlinear slow positive feedback, through  $\mathcal{S}_s$ , on the membrane potential, while  $I_u$  provides ultra-slow negative feedback. These feedback pathways correspond to those provided by ionic current on membrane potential variations in biological neurons [31, 32]: fast and slow depolarization currents that support spike initiation and bursting, as well as slow and ultraslow repolarization and adaptation currents [39, 40].

Besides its current-mode nature, our neuron design departs from [19, 34] in two other fundamental aspects. First, the negative feedback loops in the proposed mixed-feedback architecture are linear, removing additional gating and saturating sigmoidal blocks. This simplification reduces circuit complexity, area, and power consumption, while minimally affecting robustness and tunability. Second, inspired by ionic current inactivation kinetics in biological

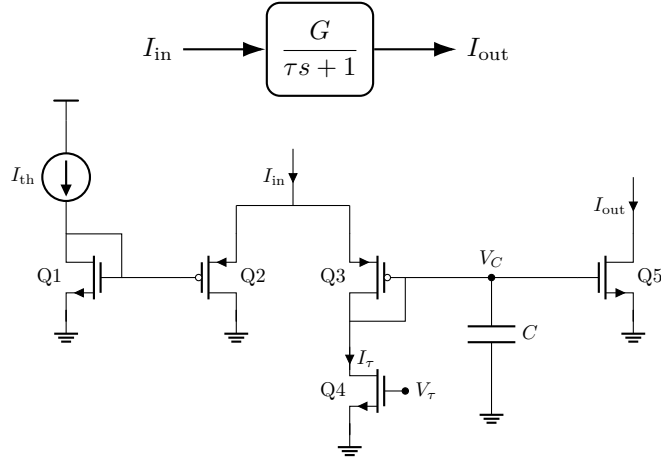


**Figure 4.** Differential-pair integrator (DPI) circuit (from [10, 38, 44, 45]). Q2-3 are the differential pair receiving the input current  $I_{in}$ . With Q1, Q2 sets the gain  $G = \frac{I_{th}}{I_\tau}$  of the circuit by diverting part of the input current depending on  $I_{th}$ , while Q3 sets the voltage  $V_C$  of the capacitor. Q4 provides the leakage current  $I_\tau$  that discharges the capacitor over time. Q5 provides an output current  $I_{out}$  depending on the capacitor voltage  $V_C$ .

neurons [39, 42, 43], our model includes a positive feedback inactivation mechanism to obtain slimmer, shorter, and more power-efficient spikes. In practice, the gains of the fast and slow nonlinear positive feedback functions are modulated by subtracting the slow  $I_s$  and ultraslow  $I_u$  currents to the fast  $I_{G_f,0}$  and slow  $I_{G_s,0}$  sigmoid gains, respectively. The modulated sigmoid gains  $I_{G_f}(t)$  and  $I_{G_s}(t)$  are defined as

$$\begin{aligned} I_{G_f}(t) &= I_{G_f,0} - I_s(t), \\ I_{G_s}(t) &= I_{G_s,0} - I_u(t). \end{aligned}$$

Because the fast dynamics are assumed to be much faster than the slower ones, the multiplicative interactions created by positive feedback inactivation has a negligible impact during the initiation of a spike but becomes significant during repolarization. By attenuating positive feedback right after a spike is generated, it lets the neuron repolarize faster, lowering power consumption per spike and making events more localized in time, without interfering with the underlying excitability and modulation properties. The effect of positive feedback inactivation is illustrated in Fig. 3, which compares simulations of spiking and bursting traces with and without inactivation.

## 2.2 Implementation of current-mode circuit blocks

To implement the current-mode low-pass filters required by the mixed-feedback architecture presented in Section 2.1, we use the differential-pair integrator (DPI) circuit [38] shown in Fig. 4. The DPI has become a staple in analog and mixed-signal neuromorphic systems due to its compact design, low power operation, and tunable gain and timescale.

Under the assumptions of subthreshold operation, and provided that the input current exceeds the leakage current ( $I_{in} > I_\tau$ ), so that the output current will eventually dominate the threshold current ( $I_{out} \gg I_{th}$ ), its dynamics can be approximated by those of a first-order low-pass filter, as expressed in (1), with a gain  $G = \frac{I_{th}}{I_\tau}$  and a time constant  $\tau = \frac{CU_T}{\kappa I_\tau}$ , where  $I_\tau = I_0 e^{\frac{\kappa V_r}{U_T}}$ ,  $I_0$  is the transistor leakage current,  $\kappa$  is the subthreshold slope factor, and  $U_T$  is the thermal voltage.

The mixed-feedback model relies on a strong separation between the different timescales. In hardware, this translates into DPI filters with time constant spanning several orders of magnitude, implemented here through scaling of the capacitor sizes. Here, we used capacitors ranging from hundreds of fF for the fast timescale to tens of pF for the ultraslow one, achieving timescales from milliseconds to hundreds of milliseconds. As will be discussed later in Section 4.1, these capacitors occupy most of the neuron’s area on chip, representing the main physical cost of faithfully implementing biologically plausible timescales.

The two nonlinear sigmoids  $\mathcal{S}_f(I_f; I_{G_f})$  and  $\mathcal{S}_s(I_s; I_{G_s})$  in the neuron model are implemented using a custom current-mode subthreshold circuit, shown in Fig. 5. This design combines a simple comparator with diode-connected transistors and a gain branch to produce a fully tunable sigmoidal current-to-current relationship. Three bias voltages (associated to bias currents through the standard subthreshold equation of NFETs in the saturation regime  $I_b = I_0 e^{\frac{\kappa V_b}{U_T}}$ ) independently

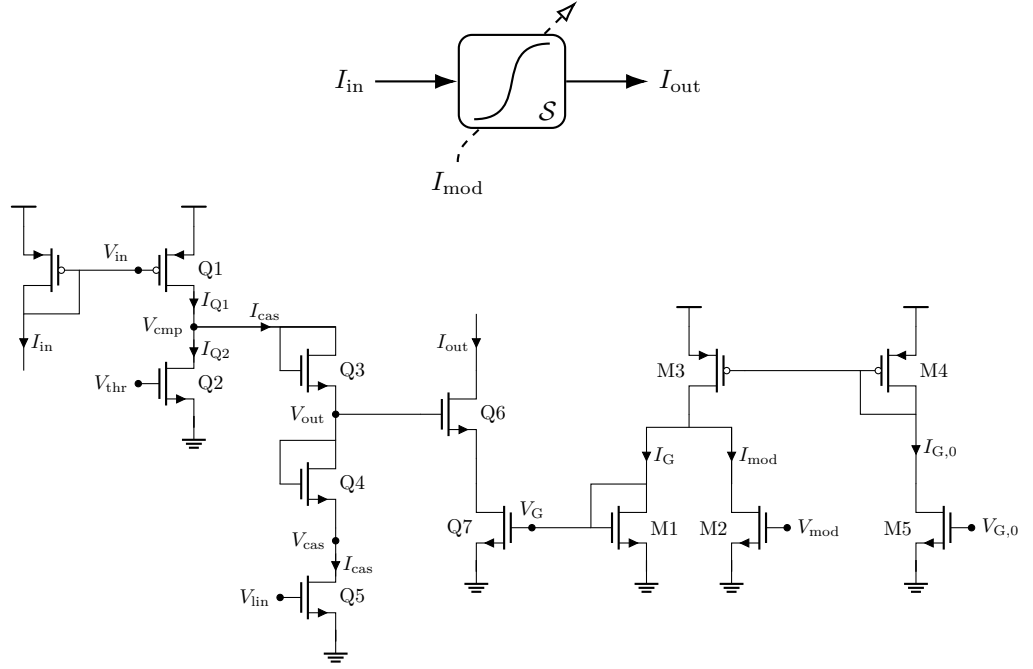


**Figure 5.** Current-mode sigmoid circuit with inactivation mechanism. Q1-2 form a simple current comparator circuit: when  $I_{in} > I_{thr}$ , the voltage  $V_{cmp}$  starts to increase. Q3-5 control the rate of increase of  $V_{cmp}$ : the higher  $V_{lin}$  is, the more current is drawn by this branch, increasing the response range of the comparator. Q6-7 set the gain of the circuit, defining the maximum output current  $I_{gain}$  at which the sigmoid saturates. The role of M1-5 is to implement the inactivation mechanism by subtracting  $I_{mod}$  from the parameter  $I_{gain}$ .

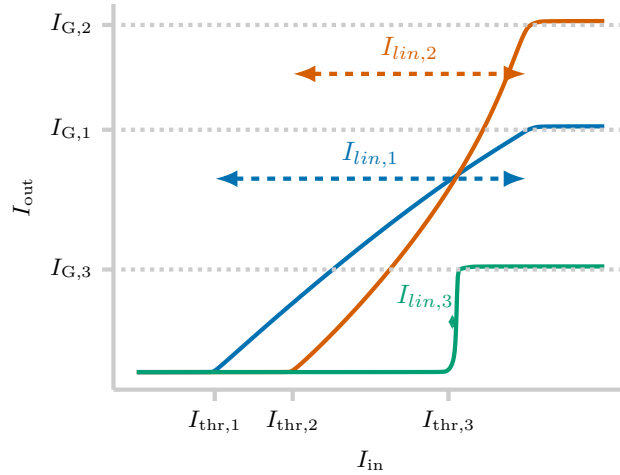


**Figure 6.** Current-mode sigmoid circuit response for different bias parameter values. The bias currents  $I_{thr}$ ,  $I_{lin}$ , and  $I_G$  accurately set the input threshold, the width of the monotonically increasing range, and the maximum output current respectively, for any combination of subthreshold bias parameters.

provide full control over the sigmoid input-output characteristic.  $V_{thr}$  sets the input threshold current  $I_{thr}$  at which the circuit starts outputting current;  $V_{lin}$  controls the size of the input current range over which the sigmoidal output is monotonically increasing and roughly linear; and  $V_G$  sets the maximum output current  $I_G$ . The effect of these three bias currents is illustrated in Fig. 6. The result is a compact, low-power, and easily tunable current-mode sigmoid function, well suited for designing neuromorphic circuits with nonlinear feedback dynamics.

The circuit shown in Fig. 5 also includes a gain modulation subcircuit that implements the positive feedback inactivation dynamics described in Section 2.1. The inactivation current  $I_{mod}$  is subtracted from the baseline gain current  $I_{G,0}$  using current mirrors, such that the effective gain bias voltage  $V_G$  fed to the sigmoid gain branch produces a gain current  $I_G(t) = I_{G,0} - I_{mod}(t)$ .

By using the DPI and sigmoid circuits, the entire mixed-feedback model presented in Fig. 2 can be implemented with only two different analog blocks, as shown in the full circuit schematic in Fig. 13, simplifying not only tuning but also chip design and layout. This modularity is a key



strength of the approach: each feedback loop is implemented using the same circuit templates, with the resulting feedback behavior controlled entirely through bias currents. As a result, the system benefits from consistent power-performance characteristics across all time scales, while enabling flexible control over excitability, adaptation, and firing regimes. The use of subthreshold current-mode design further ensures ultra-low power operation, making the neuron well suited for large-scale deployment in power-constrained neuromorphic systems.

**Current-scale invariance** Because all state variables are currents and interact through linear DPI filters and current-mode summation, the model dynamics are invariant under uniform scaling of the bias currents, provided the system operates in the subthreshold regime. In other words, neurons can be biased in the picoampere, nanoampere, or even higher subthreshold current ranges without altering their qualitative behaviors (e.g., excitability class, bursting capability). These insights will be justified in Section 2.3. Increasing the operating current reduces mismatch sensitivity at the expense of higher power consumption, while lower currents favor ultra-low-power operation. This flexibility makes the approach suitable for both energy-constrained systems and performance-critical scenarios.

**Temperature invariance** Similar arguments as for the current-scale invariance apply when considering temperature variations. Because the subthreshold currents scale with temperature, all feedback loop currents and time constants change proportionally, preserving their relative ratios. Consequently, the neuron dynamics remain qualitatively invariant, with temperature primarily rescaling the temporal evolution. This proportional scaling accounts for the temperature invariance experimentally observed in Figure 12.

### 2.3 Model tuning and theoretical analysis

To capture the continuous-time dynamics of our mixed-feedback neuron, we can leverage the structure of the model and write the input-output relationship of each low-pass filter, which yields

$$\tau_f \dot{I}_f = -I_f + G_f (\mathcal{S}_f(I_f; I_{G_f}) + \mathcal{S}_s(I_s; I_{G_s}) - I_s - I_u + I_{app}), \quad (2a)$$

$$\tau_s \dot{I}_s = -I_s + G_s I_f, \quad (2b)$$

$$\tau_u \dot{I}_u = -I_u + G_u I_f. \quad (2c)$$

These equations enable the use of the techniques introduced in [31, 32] for biophysical conductance-based models and in [34] for voltage-mode mixed-feedback circuits to analyze the emergence of spiking and bursting behaviors from the interaction of the different feedback loops in this continuous mixed-feedback model. They provide a fast and systematic way of tuning the various parameters of the model by revealing the excitability thresholds, bistable regions, and modulation of firing regimes. Practically, they allow us to skip lengthy transient simulations and tune bias voltages solely based on DC characteristics of the feedback loops.

To illustrate these techniques, we compute the steady-state "output-input" curves used in [19, 34] to analyze their mixed-feedback neurons. These curves are conceptually similar to the I-V (current-voltage) curves measured under voltage clamp experiments in neuroscience. To that end, we assume timescale separation, that is,  $\tau_f \ll \tau_s \ll \tau_u$ , and neglect the effect of positive feedback inactivation. This is a reasonable assumption since the fast (*resp.* slow) inactivation depends on the slow (*resp.* ultraslow) variable, which is negligible in the timescale of interest. We also set  $G_f = G_s = G_u = 1$ , so that the DPI circuits behave like linear leaky integrators. We can write the three steady-state curves by sequentially setting the derivatives in Eq. (2) to zero, starting from the fastest subsystem and neglecting the effect of slower variables:

$$\dot{I}_f = 0 \Leftrightarrow I_{app} = \bar{I}_f - \mathcal{S}_f(\bar{I}_f; \bar{I}_{G_f}) \quad (3a)$$

$$\dot{I}_f, \dot{I}_s = 0 \Leftrightarrow I_{app} = 2\bar{I}_s - \mathcal{S}_f(\bar{I}_s; \bar{I}_{G_f}) - \mathcal{S}_s(\bar{I}_s; \bar{I}_{G_s}) \quad (3b)$$

$$\dot{I}_f, \dot{I}_s, \dot{I}_u = 0 \Leftrightarrow I_{app} = 3\bar{I}_u - \mathcal{S}_f(\bar{I}_u; \bar{I}_{G_f}) - \mathcal{S}_s(\bar{I}_u; \bar{I}_{G_s}) \quad (3c)$$

Examples of these curves and the resulting simulated neuron activity are shown in Fig. 7. Each steady-state curve represents the set of equilibrium points of the neuron at a given timescale, obtained by freezing the slower variables. The slope of these curves directly indicates the stability of the corresponding equilibria: regions of positive slope correspond to stable fixed points, while

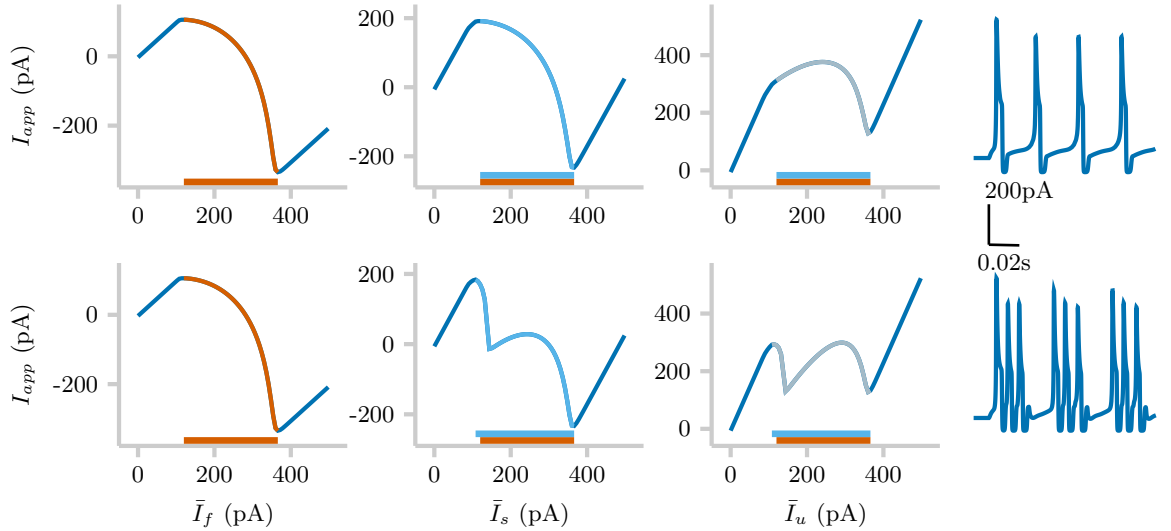


**Figure 7.** Examples of steady-state curves (left) of our mixed-feedback model and the corresponding neuron responses (right). The red (*resp.* cyan) regions are the bistability region of the fast (*resp.* slow) subsystems. When the slow bistability region is entirely contained within the fast one (top), the neuron can only exhibit tonic spiking. When the slow bistability region threshold comes before the fast one (bottom), the neuron becomes capable of bursting. The y-axis of the ultraslow curve indicates which input current will put the neuron in a certain region.

regions of negative slope indicate local instability and potential bistability. By comparing the relative positions of the fast, slow, and ultraslow curves, one can immediately infer whether the neuron will exhibit tonic spiking, bursting, or purely passive behavior. A region of negative slope in the fast steady-state curve translates the existence of positive feedback, responsible for spike initiation. If a portion of negative slope appears in the slow steady-state curve before the fast excitability threshold, it shows a bistability between tonic spiking and silence, from which bursting can arise when an ultraslow variable slowly drives the system across this bistable region. A monotonically increasing ultraslow steady-state curve guarantees that, at the slowest timescale, the system is monotonically stable, ensuring that it will go back to rest after a spike or a burst.

This geometric interpretation provides a powerful visual tool to understand how feedback interactions and timescale separation generate complex dynamics. Moreover, these steady-state curves only depend on  $\mathcal{S}_f$  and  $\mathcal{S}_s$ , and can therefore be analyzed by simply simulating the DC characteristics of the two sigmoid circuits.

From a theoretical standpoint, Eq. (2) also predicts the scaling properties of the model. Because all state variables and parameters appear as currents and interact through linear current-mode filters, the dynamics remain invariant under uniform scaling of the bias currents, explaining the current-range invariance discussed in Section 2.2. Likewise, under subthreshold operation, temperature affects all transistor currents through the same exponential dependence  $I \propto e^{\kappa V/U_T}$ ; hence, the ratios between feedback currents are preserved, ensuring functional robustness across temperature variations. These invariance properties, intrinsic to the mixed-feedback current-mode formulation, contribute to the robustness of the proposed neuromorphic architecture.

### 3 Experimental results

To validate the proposed mixed-feedback neuron architecture and its current-mode implementation, we fabricated and experimentally characterized the silicon neuron under various operating conditions. This section demonstrates that the fabricated circuit reproduces the key behaviors predicted by the model, including spiking and bursting dynamics, robust neuromodulation, and low-power operation. We first describe the experimental setup and measurement methodology, followed by an analysis of the basic excitability and modulation properties. Specifically, we demonstrate the emergence of bursting through parameter tuning, and highlight the relationship between input strength and firing frequency, both for slow (Type-I) tonic spiking, and tonic bursting. We then report power consumption simulations, detailing the reported metrics for different firing patterns and frequencies. Finally, we present the results of a temperature robustness experiment, showing how our mixed-feedback neuron behaves at various operating temperatures.



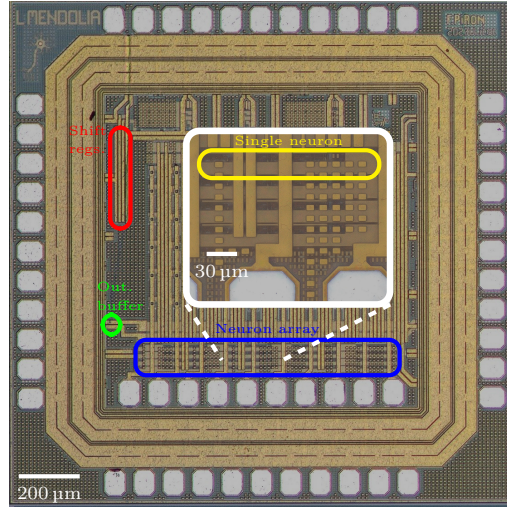


**Figure 8.** Micrograph of the prototype chip (2023) containing the test mixed-feedback neurons. Blue: array of the 16 mixed-feedback neurons. Green: output buffer stage. Red: shift registers. Inset: zoom on 4 mixed-feedback neurons stacked on top of one another. Yellow: a single neuron.

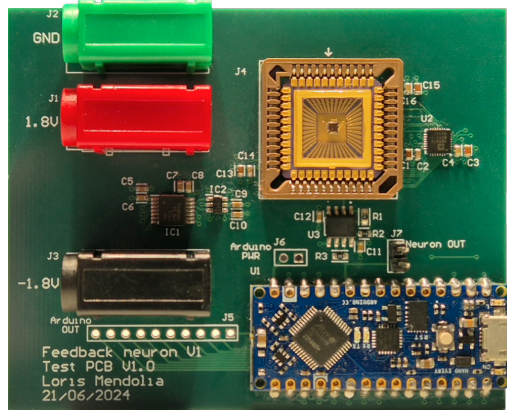


**Figure 9.** Custom PCB used for characterization of the on-chip mixed-feedback neurons. The board hosts the fabricated CMOS die (center), an external 12-bit DAC (AD5674) for bias generation, and an operational amplifier configured as a feedback ammeter for on-board current-to-voltage conversion. A microcontroller (Arduino Nano Every) controls the on-chip multiplexer for output selection and the programming of the DAC for bias generation. Output signals were acquired with an oscilloscope (Analog Discovery 3) for data acquisition.

### 3.1 Experimental setup

An array of 16 mixed-feedback neurons was fabricated on a test chip in a 180 nm CMOS X-FAB process. An active area of  $750 \times 90 \mu\text{m}^2$  was dedicated to this end. A micrograph of the fabricated chip is shown in Fig. 8, highlighting the neuron array, control logic, and output. All neurons share a common set of 12 bias voltages, generated by an external digital-to-analog converter (DAC) (an Analog Devices AD5674 12-bit, 16-channel DAC). A single analog output is provided through a transmission gate multiplexer, controlled by on-chip shift registers. The transmission gates allow the connection of one of the three internal currents ( $I_f$ ,  $I_s$ , or  $I_u$ ) of one neuron at a time to an output buffer stage, injecting an amplified analog copy of the selected current directly to the output pad, ensuring a reliable off-chip readout of the pA or nA internal currents.

The output current is converted into a voltage on the test printed circuit board (PCB) (presented in Fig. 9) using a precision operational amplifier in feedback ammeter configuration. This configuration allows to easily achieve different gains as required. After a second amplification stage using an inverting amplifier, the resulting voltage is measured by a digital oscilloscope (Digilent Analog Discovery 3, 14-bit resolution at up to 125 MS/s, 30 MHz bandwidth) enabling a highly accurate acquisition of the neural traces. An Arduino Nano Every is mounted on the PCB to configure the shift registers and the DAC and can optionally stream output data. All results presented here were acquired using the oscilloscope for improved accuracy and flexibility. Unless otherwise stated, all measurements were performed at room temperature and at the nominal supply voltage of 1.8 V.

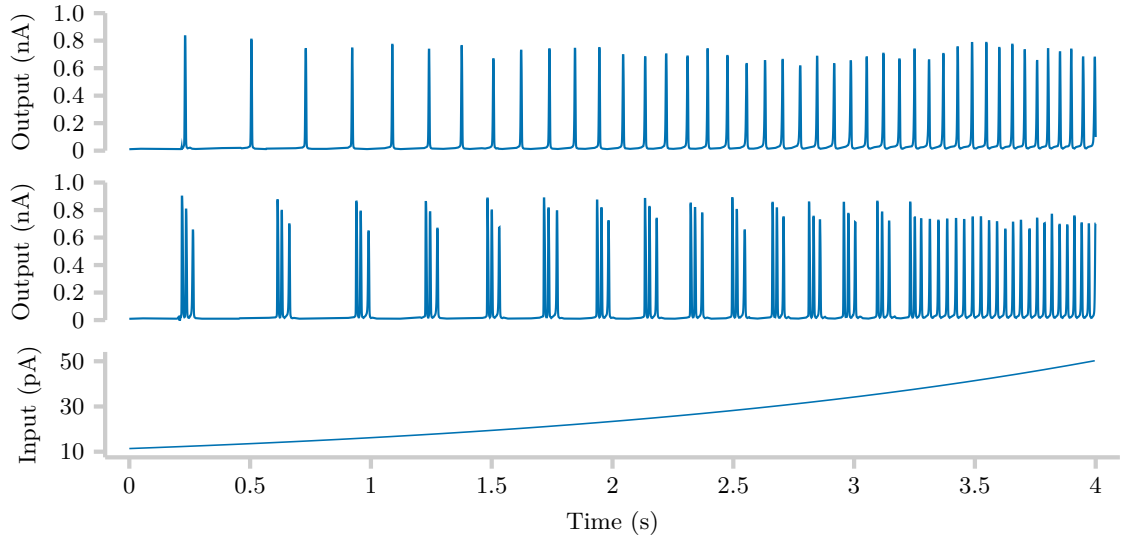


**Figure 10.** Measured neuron responses to increasing input current (bottom), in spiking (top) and bursting (middle) configurations. The neuron exhibits tonic excitability, showing firing frequencies increasing with input current in both modes, starting as low as a few Hz.

### 3.2 Measured dynamics in silicon

To validate and characterize our neuron’s behavior in silicon, we performed various measurements on the fabricated test chip. These experiments aim to confirm the neuron’s ability to robustly produce and switch between different firing regimes as predicted by the model mixed-feedback theoretical analysis. Extensive experimental exploration was performed, with experiments run several times on different days, different neurons and different bias baselines, ensuring the consistency of qualitative results. In addition, simulated power consumption metrics are reported to benchmark the energy per spike in spiking and bursting regimes, and to quantify the baseline power draw at rest.

**3.2.1 Response to exogenous input currents** Figure 10 shows the response of an on-chip neuron to an increasing input current. In both tonic spiking (top) and bursting (middle) regimes, the neuron exhibits a consistent increase in firing activity with the input, as expected from the mixed-feedback model. Despite the different internal dynamics, in both configurations the neuron responds in a consistent and reproducible way. In line with biological neurons, the spiking and bursting frequency of our neuron increases in response to an increasing exogenous input. In bursting regime and for sufficiently large applied currents, the bursts eventually overlap and the neuron transitions from bursting to fast spiking, once again in line with biological neurons.

**3.2.2 Response to neuromodulatory inputs** Figure 11 demonstrates the neuromodulation capabilities of the fabricated neuron by varying the slow positive feedback gain  $I_{G_s}$  while keeping the input current constant. As the neuromodulation parameter is incrementally increased, the neuron smoothly transitions from a tonic spiking to a tonic bursting regime, with progressively longer burst durations and more spikes per burst. These measurements illustrate how neuromodulatory tuning of a single bias current enables a smooth and predictable transition between firing regimes. Bursting characteristics, such as interburst period or spikes per burst, are directly and predictably modulated through  $I_{G_s}$ .

The observed neuromodulation dynamics are consistent with the theory of slow positive feedback: increasing the slow gain increases the slow current’s contribution to spike and burst excitability without interfering with the fast positive feedback responsible for the spike generation itself. The neuromodulatory transition achieved here is analogous to the ones observed in biophysical conductance models by increasing the maximal conductance of slow regenerative ionic currents, which create slow positive feedback on membrane potential variations [31, 32, 46].

Together, the measurements presented in Figs. 10 and 11 establish the neuron’s ability to robustly operate in both tonic spiking and bursting modes, with tunable transitions between the two. Our hardware neuron exhibits tunable excitability across a wide input dynamic range, with interpretable and reliable spiking mode control via specific bias currents. The control of bursting through a single (slow positive feedback) bias illustrated here is only one out of the many

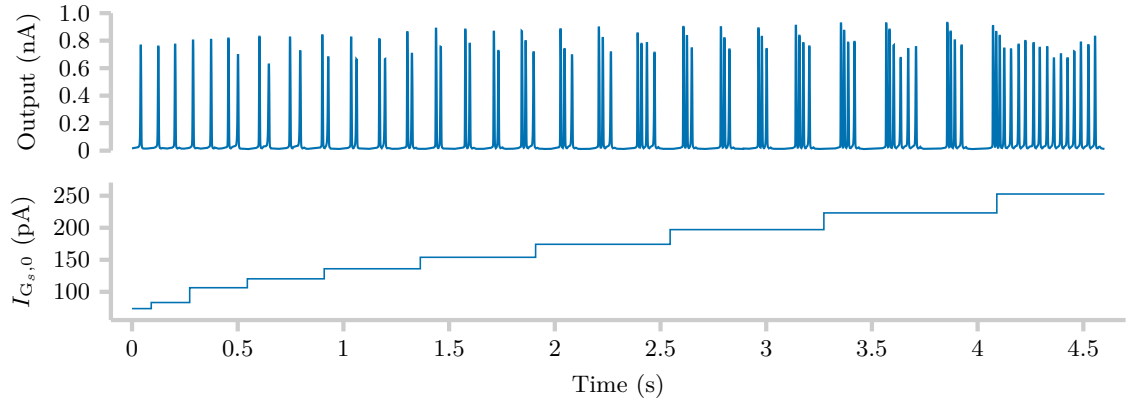


**Figure 11.** Measured neuromodulation from spiking to bursting (top) through an increase in slow positive feedback  $I_{G_{s,0}}$  (bottom). The neuron undergoes a smooth transition from spiking to bursting, with a gradual increase in the number of spikes per burst and a consistent inter-burst interval.

neuromodulatory pathways that can be explored and achieved in the proposed current-mode neuromorphic design.

As already remarked in Section 2.3, the neuron dynamics are preserved under a uniform scaling of all bias currents. This is a direct consequence of the current-mode mixed-feedback implementation: as long as the system remains in subthreshold and steady-state relationships are preserved, all time constants and feedback loops scale proportionally with bias currents. As a result, operating the neuron at 100 pA or 100 nA yields the same qualitative behaviors, from tonic spiking to bursting, with a tunable trade-off between energy efficiency and mismatch sensitivity.

**3.2.3 Simulated power consumption** SPICE simulations were used to estimate the power consumption of our neuron (based on a revised layout and transistor sizing reported in Table 2 optimized for mismatch, relative to the version implemented in the first test chip). The reported metrics exclude bias generation, digital control, and output circuitry, and focus solely on the neuron circuit described in Section 2. Under the same bias conditions used throughout the measurements in this section, a neuron consumes approximately 3 nW at rest (zero input), with instantaneous power momentarily rising to 10 nW during spike generation.

In Type-I tonic spiking at 23 Hz, the dissipation over a half-second window of continuous analog activity, including input integration, spike generation, frequency adaptation and other subthreshold dynamics, is 217 pJ/spike. After modulation to reach tonic bursting with 3 spikes per burst at 18 bursts per second, the average dissipation drops to 90 pJ/spike. As the tonic spiking frequency is increased, the dissipation drops, down to 101 pJ/spike at 50 Hz, and 41 pJ/spike at 160 Hz. These results highlight the neuron’s low-power operation across multiple dynamical states, with increasing energy efficiency at higher spiking rates.

### 3.3 Stability of the mixed-feedback model over time and temperature

To assess the robustness of our mixed-feedback neuron to environmental variations, we characterized the test chip’s response across a wide temperature range using a climatic chamber. Proper measures were taken to ensure temperature stabilization with a thermal camera, and to stay within the operating temperature range of the DAC used to generate bias voltages, also monitored throughout the experiment to ensure they remained constant.

Fig. 12 reports the evolution of the spiking and bursting frequency (measured as the inverse of the period between the start of two bursts) of two representative neurons against temperature. In both cases, frequency increases gradually with temperature, but the overall spiking and bursting behaviors remain robust and qualitatively unchanged. The neuron responses at higher temperatures effectively correspond to sped-up or time-compressed versions of those at lower temperatures, a behavior analogous to the temperature robustness observed in biological neurons of species that experience large temperature variations, such as crabs [47, 48]. This observation further emphasizes the biophysical realism of our proposed mixed-feedback design.

Quantitatively, the measured spiking and inter-burst frequency increased from approximately 0.5 Hz at 5 °C to 25 Hz at 45 °C. These changes remained smooth and monotonic, without any loss of excitatory behavior or irregular activity. Across multiple trials and bias conditions, no

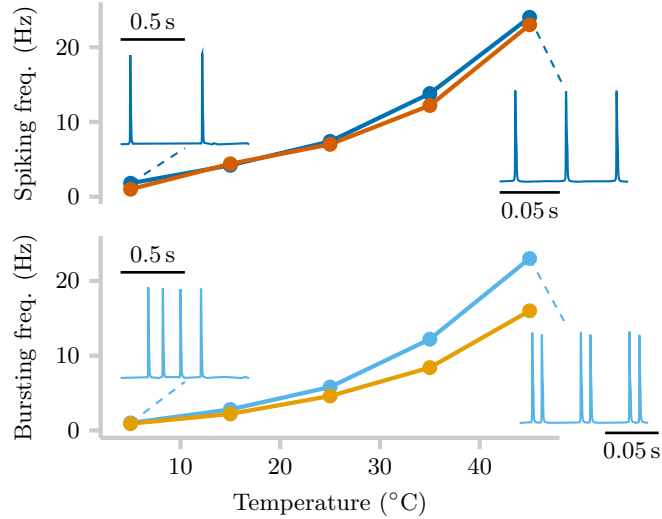


**Figure 12.** Measured variation in spiking (top) and bursting frequency (inverse of the period between the start of two bursts, bottom) of two different neurons as a function of ambient temperature, with representative output traces at two extreme temperatures. Frequency increases with temperature and follows a comparable trajectory across neurons and firing regimes. The recorded waveforms compress in time and speed up but remain in the same qualitative firing regime, confirming temperature-robust dynamics. The bursting neuron goes from 4-spike bursts at 5 °C to 2-spike bursts at 45 °C due to the sped up ultraslow dynamics.

degradation or drift was observed over repeated heating-cooling cycles, confirming the long-term stability and repeatability of the mixed-feedback neuron dynamics.

The observed frequency increase arises naturally from transistor-level temperature effects. As temperature increases, the thermal voltage  $U_T = kT/q$  and the carrier mobility  $\mu$  both change, resulting in higher subthreshold currents for identical gate bias conditions. In the DPI filters, this results in proportionally faster charging and discharging, effectively reducing the time constants of the fast, slow, and ultraslow timescales. Otherwise, since all bias voltages are set from the same external source, changes in currents scale proportionally across all feedback loops, preserving the relative strength of the fast, slow, and ultraslow feedback pathways. As a result, the mixed-feedback neuron maintains its excitability regime, while its temporal dynamics accelerate uniformly. Note that, in the bursting regime, the number of spikes per burst decreases at higher temperatures. This is consistent with our model, since the ultraslow negative feedback accelerates with temperature without an accompanying positive component to counterbalance it. Importantly, the interplay between the fast and slow timescales which gives rise to bursting remains unaffected and the neuron maintains its excitability type despite the change in burst length.

Overall, the mixed-feedback architecture provides an intrinsic form of temperature and bias self-regulation: when environmental conditions shift, the system’s internal currents scale coherently, preserving its qualitative behavior without requiring external compensation. This property further enhances the stability and robustness of the proposed model.

## 4 Discussion

### 4.1 Comparison of state-of-the-art bursting silicon neurons

To position our silicon neuron implementation alongside the state-of-the-art, we present a comparative overview of silicon neurons capable of generating bursting dynamics in the literature in Section 4.1. Unlike most prior work, which predominantly relies on voltage-mode implementations and simplified models such as the Izhikevich or AdEx neuron, our design offers a fully analog, current-mode implementation of the mixed-feedback model, extended here with a biologically motivated inactivation mechanism. This current-mode approach enables lower power consumption without sacrificing the richness of the dynamics, providing an efficient alternative to both digital implementations and transconductance-based analog designs. Compared to earlier works, such as the ones of Hynna [17] and Wijekoon [49], our neuron supports more diverse and biologically plausible behaviors while maintaining comparable or superior energy efficiency. The mixed-feedback model used here has been shown to uniquely exhibit a biologically consistent phase-plane structure, unlike the Izhikevich model which suffers from limited tunability [11, 50, 51].

While recent work by Liu et al. [19] has demonstrated a first silicon implementation of the mixed-feedback model in voltage mode, our current-mode architecture further improves energy

Ref.	Tech.	Impl.	Model	Biologically plausible neuromodulation	Area	Energy/Power
[17]	0.25 $\mu\text{m}$ CMOS	V-mode	T-Channel Axon-Hillock	Yes	774 $\mu\text{m}^2$	?
[49]	0.35 $\mu\text{m}$ CMOS	V-mode	Izhikevich (accelerated)	No	2800 $\mu\text{m}^2$	9 pJ/spike (8 to 40 $\mu\text{W}$ )
[45]	0.35 $\mu\text{m}$ CMOS	I-mode	AdEx	N/A	913 $\mu\text{m}^2$	7 pJ/pulse, 267 pJ/spike
[18]	0.5 $\mu\text{m}$ CMOS	V-mode	Extended Hodgkin-Huxley & Morris-Lecar	Yes	?	?
[54]	0.5 $\mu\text{m}$ CMOS	Switched capacitors	Mihalaş-Niebur	No	0.05 mm <sup>2</sup>	2.375 $\mu\text{W}$
[55]	130 nm CMOS	Mixed	I&F	No	26.5 $\mu\text{m}^2$	High (FPGA)
[28, 29]	65 nm CMOS	V-mode	AdEx (accelerated)	N/A	2352 $\mu\text{m}^2$	(790 $\pm$ 170) pJ/spike
[21]	Pt/Co <sub>3</sub> O <sub>4-x</sub> /ITO	Memristive	–	N/A	–	–
[19]	180 nm CMOS	V-mode	Mixed-feedback	Yes	2590 $\mu\text{m}^2$	697 to 969 nJ/spike
[56]	NbO <sub>2</sub> + ECRAM	Memristive	Fast-slow memristive	N/A	–	–
This work	180 nm CMOS	Analog I-mode	Mixed-feedback (w/ inactivation)	Yes	3800 $\mu\text{m}^2$	40 to 200+ pJ/spike

**Table 1.** Comparison of state-of-the-art bursting silicon neurons

efficiency (down to 45 pJ/spike at 105 Hz) and simplifies interfacing in large-scale neuromorphic systems. The relatively large area of our neuron ( $\sim 3800 \mu\text{m}^2$ ) is primarily due to the capacitors implementing the slow and ultraslow DPI filters, which are essential to separate the different timescales of the mixed-feedback model by a few orders of magnitude. This reflects a fundamental trade-off between biophysical realism and integration density. Future implementations could reduce area by combining smaller capacitors with smaller leakage currents, integrating volatile memristive devices [52, 53] or leveraging advanced technology nodes. Overall, our neuron offers a unique combination of functional richness, biological plausibility, and energy efficiency, enabled by the choice of a fully analog current-mode implementation of a robust and tunable phase-portrait-based model.

## 5 Conclusions

We presented a fully analog current-mode implementation of a biologically inspired mixed-feedback neuron model that enables robust and tunable neuromodulation in neuromorphic hardware. The proposed circuit uses two types of subthreshold current-mode blocks interconnected in a feedback configuration, and introduces a positive-feedback inactivation mechanism. The resulting neuron can be tuned using mathematical steady-state analyses, and exhibits predictable and reliable excitability and neuromodulation in simulation and hardware. A 180 nm CMOS prototype exhibits spiking, bursting and real-time neuromodulation between the two using a single bias parameter across wide temperature ranges, validating the model and demonstrating the robustness of the current-mode mixed-feedback approach to global current variations. The neuron operates at 40 to 200 pJ/spike at a 1.8 V supply, confirming ultra-low-power operation and suitability for integration into large-scale neuromorphic systems.

Future work will showcase the capabilities of networks of mixed-feedback neurons interconnected through synaptic and neuromodulatory interactions to enable adaptive signal processing and sensorimotor control application. A forthcoming chip will integrate an array of the



mixed-feedback neurons presented here, with a revised layout to minimize mismatch, and programmable synaptic connections and neuromodulatory pathways to demonstrate network-level behavioral modulation. In parallel, we will investigate closed-loop neuromodulation controllers, such as the one presented in [57], to autonomously tune bias currents and compensate for device mismatch using knowledge of the neuron’s mathematical model. Together, these developments aim to advance mixed-feedback neuromorphic hardware from single-neuron demonstrations towards adaptive and energy-efficient analog computing systems.

### Acknowledgments

We gratefully acknowledge Philipp Klein for his advice and suggestions on the neuron layout, François Piron for his work on the floorplanning of the test chip and his support during the tapeout phase, and Guillaume Drion for his feedback and advice on the modeling aspects of this work.

### Funding

This work was supported by the Belgian Government through the Federal Public Service Policy and Support grant NEMODEI, and by the HORIZON EUROPE EIC Pathfinder Grant ELEGANCE (Grant No. 101161114). Loris Mendolia is a FRIA Grantee of the Fonds de la Recherche Scientifique - FNRS. Elisabetta Chicca would like to acknowledge the financial support of the CogniGron research center and the Ubbo Emmius Funds (Univ. of Groningen).

### Author contributions

- Loris Mendolia: Conceptualization (lead), Data curation, Formal analysis (lead), Investigation (lead), Methodology (equal), Software, Visualization (lead), Writing - original draft (lead), Writing - review and editing (lead).
- Chenxi Wen: Conceptualization (supporting), Investigation (supporting), Methodology (supporting), Writing - review and editing (supporting).
- Elisabetta Chicca: Conceptualization (supporting), Investigation (supporting), Resources (supporting), Writing - review and editing (supporting).
- Giacomo Indiveri: Conceptualization (supporting), Investigation (supporting), Writing - review and editing (supporting).
- Rodolphe Sepulchre: Conceptualization (supporting), Writing - review and editing (supporting).
- Jean-Michel Redouté: Conceptualization (supporting), Funding acquisition (equal), Investigation (supporting), Project administration (equal), Resources (equal), Supervision (equal), Writing - original draft (supporting), Writing - review and editing (supporting).
- Alessio Franci: Conceptualization (lead), Formal analysis (supporting), Funding acquisition (equal), Investigation (supporting), Methodology (equal), Project administration (equal), Resources (equal), Supervision (equal), Visualization (supporting), Writing - original draft (supporting), Writing - review and editing (supporting).

### Data availability

All data that support the findings of this study are included within the article.

### Supplementary data

#### Full circuit schematic

The full schematic of the current-mode mixed-feedback neuron presented in this work is displayed in Fig. 13. Transistors dimensions and capacitor sizes used in a revised layout optimized for mismatched are reported in Table 2. The dimensions of all transistors of the test circuits used to obtain the experimental results in Section 3 of this work are  $W \times L = 3 \mu\text{m} \times 300 \text{ nm}$ .

Transistors	D <sub>f</sub> 1,2	D <sub>s,u</sub> 1,2	D3	D <sub>f</sub> 4	D <sub>s,u</sub> 4	S1	S2,5,7	S3,4,6	M1,2,5	M3,4
$W \times L$ (μm)	1 × 3	2.5 × 4	4 × 5	2 × 2	5 × 5	3 × 5	4 × 5	2 × 0.6	4 × 5	2 × 5
Capacitor						$C_f$	$C_s$	$C_u$		
Total capacitance						0.5 pF	2 pF	8 pF		

**Table 2.** Mixed-feedback neuron circuit component dimensions and values (from a mismatch-optimized layout).



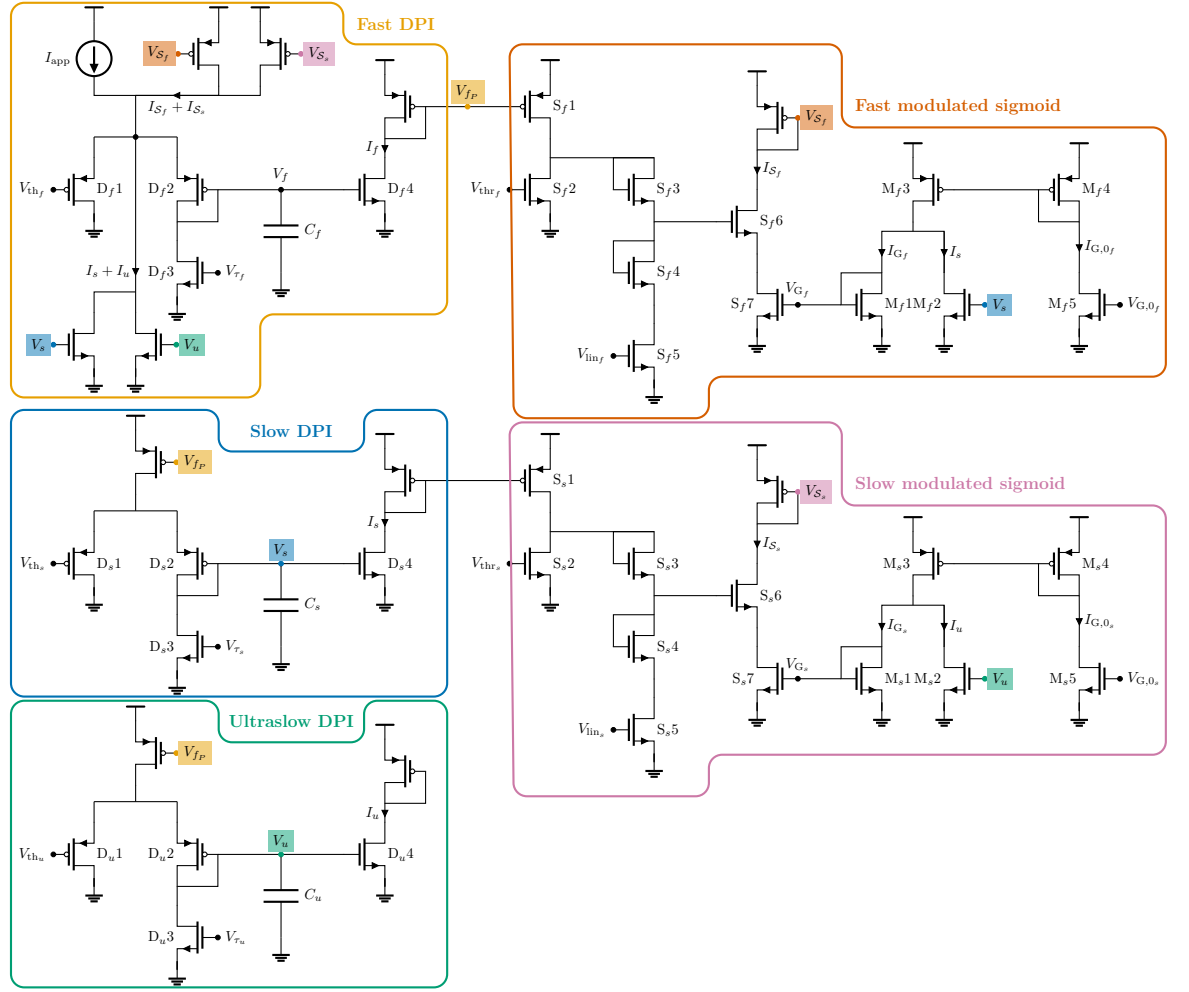


**Figure 13.** Full current-mode mixed-feedback neuron schematic, implementing the structure detailed in Section 2.1 and in Fig. 2, using the sub-circuits presented in Section 2.2 and shown in Figs. 4 and 5. All transistors operate in the subthreshold regime. The fast DPI ( $D_{f1-4}$ , yellow) models the passive membrane dynamics of the neuron. The fast current-mode sigmoid ( $S_{f1-7}$ , orange) provides fast positive feedback on the membrane potential to create the spike upstroke, corresponding to rapid sodium channel dynamics. The slow and ultraslow DPIs ( $D_{s/u1-4}$ , blue and green) introduce linear slow and ultraslow negative feedback to the system, providing repolarization and spike-frequency adaptation currents to the membrane respectively, capturing the effects of delayed-rectifier and calcium-activated potassium currents [39, 40]. The slow current-mode sigmoid ( $S_{s1-7}$ , pink) provides slow positive feedback on the membrane to create slow regenerative dynamics, mimicking low-threshold calcium currents that support bursting or regenerative depolarization. The positive feedback inactivation circuits ( $M_{f/s1-5}$ ) in the sigmoid blocks subtract copies of the slow and ultraslow currents from the base gain current of the fast and slow sigmoids respectively, inspired by biological sodium channel inactivation observed following spike initiation [43]. All unlabeled transistors are part of current mirrors that copy the currents associated to the highlighted gate voltages to implement the various feedback loops of the model.

## References

- [1] C. I. Bargmann, “Beyond the connectome: how neuromodulators shape neural circuits,” *BioEssays: News and Reviews in Molecular, Cellular and Developmental Biology*, vol. 34, pp. 458–465, June 2012.
- [2] E. Marder, “Neuromodulation of Neuronal Circuits: Back to the Future,” *Neuron*, vol. 76, pp. 1–11, Oct. 2012.
- [3] M. C. Avery and J. L. Krichmar, “Neuromodulatory Systems and Their Interactions,” *Frontiers in Neural Circuits*, vol. 11, p. 108, Dec. 2017.
- [4] G. Drion, A. Franci, and R. Sepulchre, “Cellular switches orchestrate rhythmic circuits,” *Biological Cybernetics*, vol. 113, pp. 71–82, Apr. 2019.

- [5] D. A. McCormick and M. P. Nusbaum, “Editorial overview: Neuromodulation: Tuning the properties of neurons, networks and behavior,” *Current opinion in neurobiology*, vol. 29, pp. iv–vii, Dec. 2014.
- [6] C. Bartolozzi, G. Indiveri, and E. Donati, “Embodied neuromorphic intelligence,” *Nature Communications*, vol. 13, p. 1024, Feb. 2022.
- [7] S. Sherman, “Tonic and burst firing: dual modes of thalamocortical relay,” *Trends in Neurosciences*, vol. 24, pp. 122–126, Feb. 2001.
- [8] C. Mead, “Neuromorphic electronic systems,” *Proceedings of the IEEE*, vol. 78, pp. 1629–1636, Oct. 1990.
- [9] G. Indiveri, “Neuromorphic is dead. long live neuromorphic,” *Neuron*, pp. 1–4, Oct. 2025.
- [10] E. Chicca, F. Stefanini, C. Bartolozzi, and G. Indiveri, “Neuromorphic Electronic Circuits for Building Autonomous Cognitive Systems,” *Proceedings of the IEEE*, vol. 102, pp. 1367–1388, Sept. 2014.
- [11] C. D. Schuman, T. E. Potok, R. M. Patton, J. D. Birdwell, M. E. Dean, G. S. Rose, and J. S. Plank, “A Survey of Neuromorphic Computing and Neural Networks in Hardware,” May 2017. arXiv:1705.06963 [cs].
- [12] E. O. Neftci, “Data and Power Efficient Intelligence with Neuromorphic Learning Machines,” *iScience*, vol. 5, pp. 52–68, July 2018.
- [13] J.-Q. Yang, R. Wang, Y. Ren, J.-Y. Mao, Z.-P. Wang, Y. Zhou, and S.-T. Han, “Neuromorphic Engineering: From Biological to Spike-Based Hardware Nervous Systems,” *Advanced Materials*, vol. 32, no. 52, p. 2003610, 2020.
- [14] C.-S. Poon and K. Zhou, “Neuromorphic Silicon Neurons and Large-Scale Neural Networks,” *Frontiers in Neuroscience*, vol. 5, p. 108, Sept. 2011.
- [15] C. S. Thakur, J. L. Molin, G. Cauwenberghs, G. Indiveri, K. Kumar, N. Qiao, J. Schemmel, R. Wang, E. Chicca, J. Olson Hasler, J.-s. Seo, S. Yu, Y. Cao, A. van Schaik, and R. Etienne-Cummings, “Large-Scale Neuromorphic Spiking Array Processors: A Quest to Mimic the Brain,” *Frontiers in Neuroscience*, vol. 12, p. 891, Dec. 2018.
- [16] T. Wunderlich, A. F. Kungl, E. Müller, A. Hartel, Y. Stradmann, S. A. Aamir, A. Grübl, A. Heimbrecht, K. Schreiber, D. Stöckel, C. Pehle, S. Billaudelle, G. Kiene, C. Mauch, J. Schemmel, K. Meier, and M. A. Petrovici, “Demonstrating advantages of neuromorphic computation: A pilot study,” *Frontiers in Neuroscience*, vol. 13, 2019.
- [17] K. M. Hynna and K. Boahen, “Silicon neurons that burst when primed,” in *2007 IEEE International Symposium on Circuits and Systems (ISCAS)*, pp. 3363–3366, May 2007. ISSN: 2158-1525.
- [18] T. Yu, T. J. Sejnowski, and G. Cauwenberghs, “Biophysical Neural Spiking, Bursting, and Excitability Dynamics in Reconfigurable Analog VLSI,” *IEEE Transactions on Biomedical Circuits and Systems*, vol. 5, pp. 420–429, Oct. 2011.
- [19] K. Liu, S. Hashemkhani, J. Rubin, and R. Kubendran, “BioNN: Bio-Mimetic Neural Networks on Hardware Using Nonlinear Multi-Timescale Mixed-Feedback Control for Neuromodulatory Bursting Rhythms,” *IEEE Journal on Emerging and Selected Topics in Circuits and Systems*, vol. 13, pp. 914–926, Dec. 2023.
- [20] X. Li, Q. Chen, and F. Xue, “Bursting dynamics remarkably improve the performance of neural networks on liquid computing,” *Cognitive Neurodynamics*, vol. 10, pp. 415–421, Oct. 2016.
- [21] H. Liu, X. Zhu, Z. Guo, R. He, X. Li, Q. Sun, X. Ye, C. Sun, Y. Tian, and R.-W. Li, “Artificial Spiking Neuron with Bursting Dynamics for Noise-Resistant Neuromorphic Coding,” *ACS Applied Electronic Materials*, vol. 5, pp. 3454–3461, June 2023.
- [22] M. Stuck, X. Wang, and R. Naud, “A burst-dependent algorithm for neuromorphic on-chip learning of spiking neural networks,” *Neuromorphic Computing and Engineering*, vol. 5, p. 014010, Feb. 2025.

- [23] J. Mei, A. Rodriguez-Garcia, D. Takeuchi, G. Wainstein, N. Hubig, Y. Mohsenzadeh, and S. Ramaswamy, “Improving the adaptive and continuous learning capabilities of artificial neural networks: Lessons from multi-neuromodulatory dynamics,” Jan. 2025. arXiv:2501.06762 [q-bio].
- [24] A. J. Ijspeert, “Central pattern generators for locomotion control in animals and robots,” *Neural Networks*, vol. 21, pp. 642–653, May 2008.
- [25] E. Donati, R. Krause, and G. Indiveri, “Neuromorphic Pattern Generation Circuits for Bioelectronic Medicine,” Feb. 2021. arXiv:2102.09630 [cs].
- [26] A. Athota, B. Caccam, R. Kochis, A. Ray, G. Cauwenberghs, and F. D. Broccard, “Neuromorphic Instantiation of Spiking Half-Centered Oscillator Models for Central Pattern Generation,” in *2021 43rd Annual International Conference of the IEEE Engineering in Medicine & Biology Society (EMBC)*, pp. 6703–6706, Nov. 2021.
- [27] P. Lopez-Osorio, A. Patiño-Saucedo, J. P. Dominguez-Morales, H. Rostro-Gonzalez, and F. Perez-Peña, “Neuromorphic adaptive spiking CPG towards bio-inspired locomotion,” *Neurocomputing*, vol. 502, pp. 57–70, Sept. 2022.
- [28] C. Pehle, S. Billaudelle, B. Cramer, J. Kaiser, K. Schreiber, Y. Stradmann, J. Weis, A. Leibfried, E. Müller, and J. Schemmel, “The BrainScaleS-2 accelerated neuromorphic system with hybrid plasticity,” Feb. 2022. arXiv:2201.11063 [cs].
- [29] S. A. Aamir, Y. Stradmann, P. Müller, C. Pehle, A. Hartel, A. Grübl, J. Schemmel, and K. Meier, “An Accelerated LIF Neuronal Network Array for a Large-Scale Mixed-Signal Neuromorphic Architecture,” *IEEE Transactions on Circuits and Systems—Part I: Regular Papers*, vol. 65, pp. 4299–4312, Dec. 2018.
- [30] O. Richter, C. Wu, A. M. Whatley, G. Köstinger, C. Nielsen, N. Qiao, and G. Indiveri, “DYNAP-SE2: a scalable multi-core dynamic neuromorphic asynchronous spiking neural network processor,” *Neuromorphic Computing and Engineering*, vol. 4, p. 014003, Jan. 2024. Publisher: IOP Publishing.
- [31] A. Franci, G. Drion, V. Seutin, and R. Sepulchre, “A Balance Equation Determines a Switch in Neuronal Excitability,” *PLOS Computational Biology*, vol. 9, p. e1003040, May 2013.
- [32] G. Drion, A. Franci, J. Dethier, and R. Sepulchre, “Dynamic Input Conductances Shape Neuronal Spiking,” *eneuro*, vol. 2, pp. ENEURO.0031–14.2015, Jan. 2015.
- [33] F. Castaños and A. Franci, “Implementing robust neuromodulation in neuromorphic circuits,” *Neurocomputing*, vol. 233, pp. 3–13, Apr. 2017.
- [34] L. Ribar and R. Sepulchre, “Neuromodulation of Neuromorphic Circuits,” *IEEE Transactions on Circuits and Systems—Part I: Regular Papers*, vol. 66, pp. 3028–3040, Aug. 2019.
- [35] R. Sepulchre, G. Drion, and A. Franci, “Control Across Scales by Positive and Negative Feedback,” *Annual Review of Control, Robotics, and Autonomous Systems*, vol. 2, pp. 89–113, May 2019.
- [36] A. Rubino, C. Livanelioglu, N. Qiao, M. Payvand, and G. Indiveri, “Ultra-Low-Power FDSOI Neural Circuits for Extreme-Edge Neuromorphic Intelligence,” *IEEE Transactions on Circuits and Systems I: Regular Papers*, vol. 68, pp. 45–56, Jan. 2021.
- [37] A. Rubino, *Mixed-Signal Neuromorphic Circuits and Systems for Extreme-Edge Computing*. PhD thesis, University of Zurich, Zürich, Mar. 2025.
- [38] C. Bartolozzi, S. Mitra, and G. Indiveri, “An ultra low power current-mode filter for neuromorphic systems and biomedical signal processing,” in *2006 IEEE Biomedical Circuits and Systems Conference*, pp. 130–133, Nov. 2006. ISSN: 2163-4025.
- [39] A. L. Hodgkin and A. F. Huxley, “A quantitative description of membrane current and its application to conduction and excitation in nerve,” *The Journal of Physiology*, vol. 117, pp. 500–544, Aug. 1952.
- [40] E. M. Izhikevich, *Dynamical Systems in Neuroscience: The Geometry of Excitability and Bursting*. The MIT Press, July 2006.

- [41] S. DeWeerth, L. Nielsen, C. Mead, and K. Astrom, “A simple neuron servo,” *IEEE Transactions on Neural Networks*, vol. 2, pp. 248–251, Mar. 1991.
- [42] B. Hille, *Ion Channels of Excitable Membranes*. Sinauer Associates Inc., U.S., 2001.
- [43] Y. Zang, E. Marder, and S. Marom, “Sodium channel slow inactivation normalizes firing in axons with uneven conductance distributions,” *Current Biology*, vol. 33, pp. 1818–1824.e3, May 2023.
- [44] C. Bartolozzi and G. Indiveri, “Synaptic dynamics in analog VLSI,” *Neural Computation*, vol. 19, pp. 2581–2603, Oct. 2007.
- [45] P. Livi and G. Indiveri, “A current-mode conductance-based silicon neuron for address-event neuromorphic systems,” in *2009 IEEE International Symposium on Circuits and Systems*, pp. 2898–2901, May 2009. ISSN: 2158-1525.
- [46] A. Franci, G. Drion, and R. Sepulchre, “Robust and tunable bursting requires slow positive feedback,” *Journal of Neurophysiology*, vol. 119, pp. 1222–1234, Mar. 2018.
- [47] L. S. Tang, A. L. Taylor, A. Rinberg, and E. Marder, “Robustness of a Rhythmic Circuit to Short- and Long-Term Temperature Changes,” *Journal of Neuroscience*, vol. 32, pp. 10075–10085, July 2012.
- [48] J. Ratliff, A. Franci, E. Marder, and T. O’Leary, “Neuronal oscillator robustness to multiple global perturbations,” *Biophysical Journal*, vol. 120, pp. 1454–1468, Apr. 2021. Publisher: Elsevier.
- [49] J. H. B. Wijekoon and P. Dudek, “Compact silicon neuron circuit with spiking and bursting behaviour,” *Neural Networks*, vol. 21, pp. 524–534, Mar. 2008.
- [50] G. Drion, A. Franci, V. Seutin, and R. Sepulchre, “A Novel Phase Portrait for Neuronal Excitability,” *PLOS ONE*, vol. 7, no. 8, p. e41806, 2012.
- [51] K. Jacquerie and G. Drion, “Robust switches in thalamic network activity require a timescale separation between sodium and T-type calcium channel activations,” *PLOS Computational Biology*, vol. 17, no. 5, p. e1008997, 2021.
- [52] R. Berdan, E. Vasilaki, A. Khiat, G. Indiveri, A. Serb, and T. Prodromakis, “Emulating short-term synaptic dynamics with memristive devices,” *Scientific Reports*, vol. 6, no. 18639, pp. 1–9, 2016.
- [53] T. Moon, K. Soh, J. S. Kim, J. E. Kim, S. Y. Chun, K. Cho, J. J. Yang, and J. H. Yoon, “Leveraging volatile memristors in neuromorphic computing: from materials to system implementation,” *Materials Horizons*, vol. 11, no. 20, pp. 4840–4866, 2024.
- [54] F. Folowosele, T. J. Hamilton, and R. Etienne-Cummings, “Silicon Modeling of the Mihalas–Niebur Neuron,” *IEEE Transactions on Neural Networks*, vol. 22, pp. 1915–1927, Dec. 2011.
- [55] R. Wang, C. S. Thakur, T. J. Hamilton, J. Tapson, and A. Van Schaik, “A compact aVLSI conductance-based silicon neuron,” in *2015 IEEE Biomedical Circuits and Systems Conference (BioCAS)*, (Atlanta, GA, USA), pp. 1–4, IEEE, Oct. 2015.
- [56] Y. Xiao, Y. Liu, B. Zhang, P. Chen, H. Zhu, E. He, J. Zhao, W. Huo, X. Jin, X. Zhang, H. Jiang, D. Ma, Q. Zheng, H. Tang, P. Lin, W. Kong, and G. Pan, “Bio-plausible reconfigurable spiking neuron for neuromorphic computing,” *Science Advances*, vol. 11, p. eadr6733, Feb. 2025.
- [57] A. Fyon, P. Sacré, A. Franci, and G. Drion, “Reliable neuromodulation from adaptive control of ion channel expression,” *IFAC-PapersOnLine*, vol. 56, pp. 458–463, Jan. 2023.